SAND2013-9538J

Chemical Quantification of Atomic-scale EDS Maps under Thin Specimen Conditions

Ping Lu[1*], Eric Romero[1] and Quanxi. Jia[2]

[1]Sandia National Laboratories, PO Box 5800, MS 1411, Albuquerque, NM 87185-1411 USA

[2]Center for Integrated Nanotechnologies, Los Alamos National Laboratory, Los Alamos, NM 87545, USA

*Corresponding author: plu@sandia.gov

Abstract:

We report our effort to quantify atomic-scale chemical maps obtained by collecting energy-dispersive X-ray spectra (EDS) using scanning transmission electron microscopy (STEM) (STEM-EDS). Under a thin specimen condition and when the EDS scattering potential is localized, the X-ray counts from atomic columns can be properly counted by fitting Gaussian peaks at the atomic columns, and can then be used for site-by-site chemical quantification. The effects of specimen thickness and X-ray energy on the Gaussian peak-width are investigated by using $SrTiO_3$ (STO) as a model specimen. The relationship between the peak-width and spatial-resolution of an EDS map is also studied. Furthermore, the method developed by this work is applied to study a Sm-doped STO thin film and antiphase boundaries present within the STO film. We find that Sm atoms occupy both Sr and Ti sites but preferably the Sr sites, and Sm atoms are relatively depleted at the antiphase boundaries likely due to the effect of strain.

INTRODUCTION

Imaging and quantifying crystal structure at the atomic-scale by using unique chemical signals emitted from atoms, such as characteristic X-rays, provides a powerful tool to study crystal and defect structures at the atomic-sale in real-space. With the recent development of spherical aberration correction technology in transmission electron microscopy (TEM), atomic-scale chemical mapping has been demonstrated in scanning transmission electron microscopy (STEM) by scanning an angstrom-sized electron probe across a sample and collecting electron energy-loss spectra (EELS; thus STEM-EELS) (Browning et al., 1993; Kimoto et al., 2007; Bosman et al. 2007; Muller et al., 2008; Wang et al., 2008; Shah et al. 2010; Watanabe et al., 2010) or by collecting energy-dispersive X-ray spectra (EDS; thus STEM-EDS) (Allen et al., 2012; D'Alfonso et al., 2010; Chu et al., 2010; Watanabe at al., 2010; Klenov and Zide 2011; Lu et al., 2013a). Simultaneously recorded Z-contrast or high-angle annular dark-field (HAADF) images by using electrons which have been scattered through large angles after exiting specimens are often used to provide a reference image for atomic columns. STEM-EDS mapping provides several advantages over the EELS-EDS mapping including: easy interpretation with a one-to-one correspondence between image and structure, as well as the ability to cover more of the periodic table. Routine atomic-resolution microanalysis based on STEM-EDS have been demonstrated by using a microscope based on the FEI Titan^{TM} platform, which combines a high-brightness X-FEG electron source, probe spherical aberration correction technology, and quadruple windowless silicon drift EDS detectors(Von Harrach et al. 2009).

However, the attempts to quantify the chemical compositions at the atomic-scale have been very limited thus far (Kotula et al., 2012; Lu et al., 2013a). Direct quantification of chemical composition at the atomic columns, in general, is very complicated due to a variety of

effects, including electron beam spreading, channeling and dechanneling, as well as the fact that these effects are dependent on the concentration at the atomic columns (Oxley, et al., 2007; D'Alfonso et al., 2010; Allen et al., 2012) . The effects of beam spreading and dechanneling can lead to the relative contribution from neighboring columns, or so called "cross-talk", even when a fine probe is focused on a specific column of atoms. A recent study indicated that STEM-EDS imaging is an incoherent mode similar to HAADF imaging and EDS potentials are reasonably localized at the atomic columns (D'Alfonso et al., 2010). Figure 1 shows schematically the X-ray generation process in STEM-EDS under the incoherent mode consideration. The EDS signal resulting from a particular section of specimen at thickness (z) can be obtained by direct convolution of the electron wave function (Fig.1a) at that thickness with effective EDS ionization potential localized at the atomic column (Fig.1b); and integrating the contribution over specimen thickness gives rise to total X-ray signals from the specimen (Fig.1c).

Under a thin specimen condition such that the effects of dechanneling and beam spreading are small, the EDS signal can be localized to atomic columns provided that the effective EDS potential is also localized. Under such a condition, the EDS X-ray counts resulting from individual atomic columns can be approximated by fitting localized Gaussian peaks at atomic column positions (Fig.1c). Using this approximation, we have recently quantified the chemical composition of an epitaxial $(La_{0.7}Sr_{0.3})MnO_3$ (LSMO)/$BiFeO_3$ (BFO) quantum structure (Lu et al., 2013a) and intermetallic alloys at the atomic-scale (Lu et al., 2013b).

In this study, we present details of our quantification method under the thin specimen conditions. In particularly, we investigate the effects of specimen thickness and X-ray energy on atomic-scale EDS mapping and quantification, and the relationship between Gaussian peak-width (defined as full widths at half maximum (FWHM)) and spatial resolution of the chemical

map. Additionally, we apply the method to quantify the chemical composition of a Sm-doped $SrTiO_3$ (STO) thin film and an antiphase boundary in the Sm-doped STO, and find that Sm atoms occupy both Sr and Ti sites but predominately the Sr sites; and that the Sm atoms are depleted at the antiphase boundary possibly due to a strain effect.

MATERIALS AND METHODS

STO single-crystal and Sm-doped STO thin film were used for this study. The Sm-doped STO thin films are deposited by pulsed laser disposition (PLD) on STO (100) substrate. The TEM specimen was prepared by mechanical polishing, followed by Ar ion milling to perforation. A FEI Titan™ G2 80-200 STEM with a Cs probe corrector and ChemiSTEM™ technology (X-FEG™ and SuperX™ EDS with four windowless silicon drift detectors) operated at 200 kV was used in this study. For atomic-scale chemical mapping, EDS spectral images were acquired as a series of frames, where the same region was scanned multiple times. Frames were spatially drift-corrected to build up spectral image data. The instantaneous dwell time on each pixel was 100 μsec, and a typical frame size was 256x256 pixels. Spectral image collection typically took about 1800 sec, yielding a total per-pixel dwell time of about 25 msec. EDS spectral image data was acquired in the STO [001] zone axis with an electron probe of size <0.18 nm, convergence angle of 18.1 mrad, and current of ~100 pA. HAADF images were recorded under similar optical conditions using an annular detector with a collection range of 60-160 mrad.

The specimen thickness was estimated by EELS measurement (Williams and Carter 2009). Elemental maps were extracted from spectral images with selected EDS energy widows for each element. Background subtraction was performed following the steps previously described (Williams and Carter 2009). The Gaussian peak-fitting was performed using a

constrained nonlinear optimization routine available in Excel 2010 (Microsoft Corporation, Redmond, WA). The "Solver" application, which is embedded in the "Analysis ToolPak", allows for easy and flexible linear and nonlinear optimization to functions defined in the spreadsheet. To improve the signal-to-noise (S/N) ratio necessary for the calculation, a smaller EDS region within the EDS map extracted from a single spectral imaging collection was selected, and an averaged map for this region was obtained by averaging several EDS maps related to each other by the lattice vector translations in the image plane. This technique was named "lattice-averaging" for convenience.

RESULTS AND DISCUSSION

Fitting Atomic-scale EDS Maps with Gaussian Peaks

We find that atomic-scale EDS maps can be fitted with Gaussian peaks located at the atomic columns when the specimen thickness is thin. Figure 2 shows EDS maps for Sr and Ti, as well as the results from the Gaussian peak-fitting. The specimen thickness, estimated from the EELS analysis, is about 16nm for this study. Sr L_α (1.806 keV) and Ti K_α (4.510 keV) lines were used for construction of Sr (Fig.2a, the left-side) and Ti (Fig.2a, the right-side) EDS maps. To improve the S/N for the Sr and Ti maps, the maps (Fig. 2a) were lattice-averaged sixteen times using ($2a_0\vec{x}$, $2a_0\vec{y}$) as the basic translation vectors, where a_0 equals to 0.39 nm and is the unit cell constant of the STO cell, $\vec{x}$ and $\vec{y}$ are the unit vectors in the x- and y- directions. The three-dimensional (3-D) surface plots of the experimental EDS maps are shown in Fig. 2b, and along with the Gaussian peak-fitting results in Fig. 2c. During the Gaussian peak-fitting, the peak positions were fixed at the lattice positions and the peak-widths were constrained to be identical for the same element, while the peak heights at the lattice positions and peak-widths were allowed to vary. The optimal fitting was achieved when the root-mean-squared-error

(RMSE) was minimized. Figure 2d shows the 3-D surface plots of the experimental (red) and fitted (green) map (image on the left-side) and residual of the fit (image on the right-side) for the Sr L_α. The residuals appear to be randomly scattered around zero indicating that the Gaussian peak-fitting describes the EDS data accurately The RMSE for the Sr L_α fitting is about 0.06. We found that a good fit is often achieved when the RMSE is less than 0.1. The FWHM of the Gaussian peaks is 0.28 nm and 0.26 nm, for the Sr and Ti map, respectively. The peak-width for Sr is slightly boarder than that of Ti, likely due to the lower energy of X-rays (L_α line, 1.806 keV) used for the Sr mapping.

The Gaussian peak-fitting allows for the X-ray counts of each atomic column to be properly separated from its neighboring columns and counted. The X-rays counts can be used to quantify the chemical composition at each atomic site by using the Cliff-Lorimer method if the k factors are known (Cliff and Lorimer 1975).

Relationship between Gaussian Peak-width and Chemical Spatial-Resolution

In chemical mapping, the shortest lateral distance among the atomic columns of identical atoms in a crystal projection determines the required spatial-resolution necessary for resolving the projected structures. This distance is 0.39 nm for STO crystal in the [001] direction and about 0.35 nm for GaAs in [110] direction. Under the assumption that the distribution of X-ray counts arising from each atomic column follows a Gaussian function distribution when the specimen is thin, the spatial-resolution in EDS maps is then directly related to the peak-width of the Gaussian function. Figure 3 shows the calculated EDS line-profile as a function of the Gaussian peak-width defined by FWHM. For the atomic columns that are fixed at a distance D apart, increasing the peak-width leads to a decrease in the intensity modulation in the EDS line-profile as

expected. The modulation is always visible if the S/N ratio is infinite. In the presence of random noise, the modulation of signal (ΔS), or the difference between the peak and the trough in the line-profile is only detectable when it exceeds the noise N by a factor of several times. If we take ΔS > 3N as a visibility criterion, then it requires the FWHM to be less than 0.855D based on our calculation shown in Fig.3 (Note that ΔS > 5N is the Rose criterion (Rose 1948), so our requirement is somewhat less strict than that of Rose's criterion). For STO in [001], it requires the FWHM to be less than 0.33 nm in order to resolve the Sr-Sr or Ti-Ti columns that are 0.39 nm apart. The reduction of the peak-width can be achieved by reducing the size of the electron probe, the thickness of the specimen, and by choosing X-rays that are produced by a highly localized EDS ionization potential to the lattice sites. The effects of specimen thickness and X-ray energy on the peak-width are studied in the following section.

Effect of Specimen Thickness and X-ray Energy

Figure 4 shows EDS color-maps of Sr (red) and Ti (green), along with the line-profiles of Ti obtained from a thin (~17 nm) and a relatively thick (~51 nm) STO specimen, respectively. Sr L_α line (1.806 keV) and Ti K_α line (4.510 keV) were used for construction of the Sr and Ti maps. The effect due to specimen thickness on EDS mapping is clearly visible. When the specimen is thin, the color-map of Sr (red) and Ti (green) (Fig.4a) shows the Sr and Ti columns clearly. On the other hand, the color-map obtained from the thicker specimen (Fig.4b), under otherwise identical experimental conditions, shows less distinguishable Sr and Ti columns, and significant X-ray overlapping between the neighboring columns (yellowish color due to mixing red (Sr) and green (Ti)). The same conclusion can be drawn from the line-profiles of Ti K_α shown in Fig. 4c. The experimental data from the 17 nm thick specimen can be easily fitted with Gaussian peaks of a FWHM of about 0.26 nm, and the intensity modulation is clearly visible. At the specimen

thickness of about 51 nm, the peak and valley oscillation in the line-profile is much reduced, leading to a less perfect match between the experimental and fitted data, and a FWHM of about 0.37 nm for the fitted Gaussian peaks. The peak-width is wider than 0.33 nm necessary for clearly resolving Ti columns at 0.39 nm apart using the $\Delta S>3N$ visibility criterion.

Figure 5 shows the effect of X-ray energy on the Ti map. Ti K_α (4.31 keV) and L_α (0.43 keV) X-rays were used to construct the Ti maps shown in Figs. 5a and 5b, respectively. The line-profiles of the experimental and Gaussian fitted data are shown in Fig. 5c. Since Ti L_α (0.43 keV) overlaps with oxygen K_α (0.53 keV), the map of Ti L_α was obtained after deconvoluting the spectra pixel-by-pixel using reference EDS spectra from Ti metal and oxygen. It is clear from the comparison in Fig. 5 that the Ti map produced by L_α X-rays is considerably noisy due to the reduced X-ray signals as well as the broadened peaks at the atomic columns. When the Ti L_α line is used instead of the Ti K_α line, the overall X-ray counts from individual Ti columns are reduced by a factor of more than six. In addition, the FWHM of the Ti peak is also increased significantly from 0.26 nm to 0.32 nm, making it difficult to resolve the individual atomic columns. The result of this study shows that, under otherwise identical conditions, choosing the X-ray line with a lower energy will broaden the peak-width; and the broadening effect will become substantial when the energy of the X-ray is less than perhaps 1 keV.

The effects on the peak-width due to specimen thickness (Fig. 4) and X-ray energy (Fig.5) can be explained based on Fig. 1. Reduction of X-ray energy gives rise to a less localized ionizing potential, resulting in a broader X-ray distribution at the atomic columns. As the specimen becomes thicker, the effects of electron beam broadening and dechanneling become more important such that the electron wave is no longer localized at the atomic columns even when a fine electron probe is focused at the columns. The exact thickness within which the

Gaussian approximation can be applied is difficult to determine, because it is dependent on many factors including; crystal structure, electron energy, electron probe size and convergence angle, X-ray energy, and compositions of atomic columns to be quantified. In general, a larger lateral distance between atomic-columns in the project, higher electron energy, smaller electron probe and probe convergence angle, and higher X-ray energy will give rise to a larger critical thickness, within which the Gaussian peaking-fitting is valid. For STO in [001] direction we estimated the critical thickness under our experimental conditions is perhaps around 30 nm. We have limited the specimen thickness to be less than 20 nm for atomic-scale chemical quantification, well within a safe thickness range for the approximation to be valid.

It is important to point out that there is really no good reason to pick the Ti L_α line for doing Ti mapping by STEM-EDS. However, if atomic-scale mapping by STEM-EELS is designed, then the Gaussian peaks associated with the EELS analysis are expected to be relatively broad based on our analysis. This is because of less-localized EELS potentials as a result of using low-energy loss edges (for example, 0.431 keV for Ti) and small integration widows above the energy edge for the EELS analysis (Wang et al., 2008). Since all of the complicated effects associated with atomic EDS mapping, such as beam spreading, channeling, and dechanneling, are also present in atomic EELS mapping, less-localized EELS potentials demand stricter limitations on specimen thickness for quantification of atomic-scale EELS maps.

Chemical Quantification of Sm-doped STO and STO Boundaries

Here we describe our recent work on chemical quantifications of Sm-doped STO thin film deposited by PLD on a (100) STO substrate and antiphase STO boundaries formed within the STO films.

Figures 6a and 6b show the EDS color-map of Sr (red) and Ti (green), as well as a map of Sm, respectively. Sm L_α (5.635 keV) and L_β (6.204 keV and 6.586 keV) lines were combined for the construction of the Sm EDS map. The maps were lattice-averaged sixteen times by translating it across the region using $(2a_0\vec{x},\ 2a_0\vec{y})$ as the basic translation vectors. Due to an overall low concentration of Sm in the STO, the map for Sm is still quite noisy even after performing the lattice-averaging. It is clear, however, that Sm atoms predominately occupy Sr sites (or A-sites) and, are also present at the Ti sites (or B-sites). Figure 6c shows the 3-D surface plot of the Sm map, exhibiting the presence of Sm peaks at both A- and B-sites.

Following the procedures described earlier, the Sr, Ti and Sm maps were fitted with individual Gaussian peaks at the lattice sites; and the X-ray counts from the lattice sites were determined from the Gaussian peak-fitting. From that, we have determined the average chemical composition at A-sites and B-sites to be $Sm_{0.08}Sr_{0.92}$, and $Sm_{0.03}Ti_{0.97}$, respectively. Therefore, the chemical formula for the Sm-doped STO can be written as $Sm_xSr_{1-x}Sm_yTi_{1-y}O_3$ with x=0.08 and y=0.03.

Figure 7a shows a HAADF image of an antiphase boundary, which is frequently observed in the Sm-doped STO in [001] projection. The antiphase is associated with a displacement vector $\vec{R}$ of 1/2 [111], corresponding to a displacement from the corner to the center of the STO unit cell. In [001] project, the lattice image is displaced across the boundary by a displacement vector of 1/2 [110]. This displacement gives rise a double Sr-O layer at the boundary as shown schematically in Fig.7b. Figure 7c shows HAADF intensity line-profiles across the boundary obtained from the lines 1 and 2 marked in Fig. 7a. The line-profiles show that the HAADF intensities at both Sr and Ti sites decrease gradually as it approaches the

boundary, indicating a gradually reduced Sm occupancy at both Sr and Ti sites (or Sm depletion) approaching the boundary.

The Sm depletion at the antiphase boundary is confirmed by atomic-scale EDS mapping. Figure 8a shows an EDS color-map of Sr (red) and Ti (green), exhibiting the boundary with an extra layer of Sr-O atoms. The EDS line-profiles across the boundary are shown in Fig.8b, in which the Sm depletion is clearly visible. The Sm X-ray counts increase gradually as it moves away from the boundary. By fitting the line-profile with Gaussian peaks at atomic columns (Fig.8b), the X-ray counts from each atomic column can be calculated. When fitting the Sm line-profile, the FWHM of the Gaussian peak for the Sm X-ray lines (L_α and L_β) was chosen to be same as that of Ti K_α, assuming the width of the EDS scattering potential for the Sm was similar to that for the Ti. Finally, the Sm composition (in mole-fraction) was calculated site-by-site by using the Cliff-Lorimer method, and is shown in Fig. 8c. It is clear from Fig. 8c that the Sm occupancy at the Sr sites is higher than at the Ti sites; and Sm is relatively depleted at the antiphase boundary.

The observation that Sm occupies the A-sites substitutionally is not surprising, given that La atoms in La-doped STO ceramic ($La_xSr_{1-x}TiO_3$) occupy the Sr sites and could replace Sr atoms up to more than 30% in mole-fraction; and Sm belongs to same group of rare-earth elements as La but with a smaller size. What is interesting is that we find a portion of Sm atoms (~27%) occupying the Ti sites in the Sm-doped STO. This happens presumably because of the smaller size of the Sm^{3+} ions. The present study provides the first direct experimental evidence of this happening. The depletion of Sm at the antiphase boundary is most likely due to the effect of strain. The presence of the double Sr-O layer at the boundary introduces a compressive strain in the direction perpendicular to the boundary due to the relatively larger size of Sr^{2+} ions

(~0.118nm) compared to that of Ti^{4+} ions (~0.075nm). This compressive strain makes the Sm^{3+} (~0.11 nm) less favorable to be incorporated into STO lattice, leading the reduction of Sm concentration at the boundary. The Sm distribution across the boundary reflects the strain distribution across the boundary: right at the boundary where the strain is the greatest, the least amount of Sm is detected.

CONCLUSIONS

A method to quantify atomic-scale chemical maps obtained by STEM-EDS has been presented in this study. We have shown that the X-ray distribution arising from atomic columns is localized at the atomic columns when the specimen is thin such that effects due to electron beam broadening and dechanneling are minimized as well as when the X-ray ionization potential is also localized. Under such a condition, the X-ray distribution can be approximated by fitting Gaussian functions at atomic columns, and the X-ray counts from these fittings can be used for the site-by-site chemical quantification. The peak-width of the localized X-ray distribution is directly related to the spatial-resolution for the EDS mapping: the smaller the peak-width, the better the spatial-resolution is. A thin specimen, small electron probe, and high X-ray energy (>1 keV) are preferred for achieving a high-resolution EDS mapping, and are necessary for atomic-scale quantifications using our method. For the first time, atomic-scale quantification of a Sm-doped STO provides direct evidence that Sm atoms occupy substitutionally at both the Sr and Ti lattice sites but preferably the Sr sites. Atomic-scale analysis of the antiphase boundary within the STO film directly reveals the chemical structure of the STO boundary which shows the presence of a double Sr-O layer, and additionally shows a depleted Sm-distribution across the boundary as a result of the strain effect associated with the STO boundary structure.

Acknowledgements

Sandia National Laboratories is a multi-program laboratory managed and operated by Sandia Corporation, a wholly owned subsidiary of Lockheed Martin Corporation, for the US Department of Energy's National Nuclear Security Administration under contract DE-AC04-94AL85000.

References:

Allen, L. J., D'Alfonso, A.J., Freitag, B., & Klenov, D. O. (2012). Chemcial mapping at atomic resolution using energy-dispersive x-ray spectroscopy. *MRS Bulletin* **37,** 47-52.

Bosman, M., Keast, Y. J., Garcia-Munoz, J.L., D'Afonso, A. J., Findlay, S.D. & Allen, L. J. (2007). Two-dimensional mapping of chemical information at atomic resolution. *Phys. Rev. Lett*. **99**, 086102.

Browning, N.D., Chisholm, M.F. & Pennycook, S.J. (1993) Atomic-resolution chemical analysis using a scanning transmission electron microscope. *Nature* **366**, 143-146.

Chu, M.W., Liou, S.C., Chang, C.P., Choa, F.S. & Chen, C. H. (2010) Emergent chemical mapping at atomic-column resolution by energy-dispersive x-ray spectroscopy in an aberration-corrected electron microscope. *Phys, Rev. Lett*. **104**, 196101 (2010)

Cliff, G. and Lorimer, G.W. (1975). The quantitative analysis of thin specimen. *J. Microsc*. **103**, 203–207.

D'Alfonso, A.J., Freitag, , B., Klenov, V. & Allen, L.J. (2010). Atomic-resolution chemical mapping using energy-dispersive x-ray spectroscopy. *Phys. Rev.* **B 81**, 100101.

Kimoto, K., Asaka, T., Nagai, T. Saito, M., Matsui, Y. & Ishizuka, K. Element-selective imaging of atomic columns in a crystal using STEM and EELS. (2007). *Nature* **450**, 702-704.

Klenov, D.O & Zide, J. M.O. (2011). Structure of the InAlAs/InP interface by atomically resolved energy dispersive spectroscopy. *App. Phys. Lett*. **99**, 141904 (2011);

Kotula, P., Klenov, D.O. & Von Harrach, H.S. (2012). Challenges to quantitative multivariate statistical analysis of atomic-resolution X-ray spectral images, *Microsc. Microanal* **18**, 691

Lu, P., Xiong, J., Van Benthem, M. & Jia, Q.X. (2013a), Atomic-scale chemical quantification of oxide interfaces using energy-dispersive X-ray spectroscopy, *App. Phys. Lett*. **102**, 173111.

Lu, P. et al. (2013b), Direct chemical imaging and quantification of metallic alloy structures at atomic-scales by energy-dispersive X-ray spectroscopy. Submitted to *Nature Communications.*

Muller, D.A., Fitting Kourkoutis, L., Murfitt, M., Song, J. H., Hwang, H.Y., Silcox, J., Dellby, N. & Krivanek, O.L. (2008). Atomic-scale chemical imaging of composition and bonding by aberration-corrected microscopy. *Science* **319,** 1073-1076.

Oxley, M.P, Varela, M., Pennycook, T.J., Van Benthem, K., Findlay, S.D., D'Alfonso, A.J., Allen, L.J. & Pennycook, S.J. (2007). Interpreting atomic-resolution spectroscopic images. *Phys. Rev.* **B76**, 64303-64311.

Rose, A. (1948) In *Advances in Electronics* (A. Marton, ed.), Academic Press, New York, P. 131.

Shah, A. B., Ramasse, Q. M., Zhai, X. F., Wen, J. G., May, S. J., Petrov, I., Bhattacharya, A., Abbamonte, P., Eckstein, J. N. & Zuo, J. M. (2012). Probing interfacial electronic structures in atomic layer LaMnO3 and SrTiO3 superlattices. *Adv. Mater*. **22**, 1156-1160.

Von Harrach, H.S., Dona, P., Freitag, B., Soltau, H., Niculae, A. & Rohde, M. (2009). *Microsc. Microanal.* 15 (suppl.2) 208.

Wang, P., D'Alfonso, A.J., Findlay, S.D., Allen, L.J., & Bleloch, A.L. (2008). Contrast Reversal in Atomic-Resolution Chemical Mapping. *Phys. Rev. Lett.* **101**, 236102.

Watanabe, M., Kanno, M., & Okunishi, E. (2010). Atomic-resolution elemental mapping by EELS and XEDS in aberration corrected STEM. *JEOL News* **45**, 8-15.

Williams, B. & Carter C.B. (2009). Transmission electron microscopy : A textbook for materials science, 2nd edition, Springer, New York.

Figure captions:

Fig.1. Schematic showing the X-ray generation process in STEM-EDS: (a) Gaussian electron probes at different thickness (z) – beam broadening along z is illustrated, and position 1 is at the atomic column site and position 2 is away from the site; (b) effective EDS scattering potential localized at atomic column and (c) overall X-ray profile obtained by the convolution of the electron wave with the EDS scattering potential at different thicknesses and by integrating the contribution through the sample thickness.

Fig.2: (a) Sr L_α EDS map (left image) and Ti K_α EDS map (right image) extracted from STEM-EDS spectral imaging; (b) experimental and (c) Gaussian peak-fitted 3-D surface plot of Sr L_α map (left image) and Ti K_α (right image) map; (d) 3-D surface plot of experimental (red) and Gaussian peak-fitted (green) Sr L_α map (left image) and of the residual from the Gaussian fitting for Sr L_α map (right image).

Fig.3. EDS line-profiles calculated as a function of the Gaussian peak-width defined by FWHM. The Gaussian peaks are fixed periodically at the lattice sites at a distance D apart.

Fig.4. EDS color-map of Sr (red) and Ti (green) obtained under identical experimental conditions from (a) a 17 nm-thin and (b) a 51nm-thick STO specimen in [001]; (c) Ti experimental EDS line-profiles along [100] direction, along with the Gaussian peak-fitted Ti line-profiles under two specimen thicknesses. The dashed lines in (c) are the individual Gaussian peaks located at the lattice sites obtained from the fitting.

Fig.5. Ti EDS map (green) extracted using (a) Ti K_α and (b) Ti L_α; (c) Experimental EDS line-profiles along [100] direction, along with the Gaussian peak-fitted line profiles obtained using two kinds of Ti X-ray lines. The dashed lines in (c) are the individual Gaussian peaks located at the lattice sites obtained from the fitting.

Fig.6. (a) EDS color-map of Sr (red) and Ti (green); (b) EDS map of Sm; and (c) 3-D surface plot of Sm EDS map. The arrows in (c) mark the positions of A- and B-sites in STO structure in [001] direction.

Fig.7. (a) HAADF image of antiphase boundary; (b) schematic model of the antiphase boundary; and (c) the line-profiles of HAADF intensity along lines 1 and 2 marked in (a) showing the HAADF intensities at both Sr and Ti sites increase gradually as it moves away from the boundary.

Fig.8. (a) Color-map of Sr (red) and Ti (green) showing the structure of the antiphase boundary; (b) the line-profiles of Sr, Ti and Sm EDS maps across the boundary along with Gaussian peaks (dashed-lines) located at the lattice sites resulting from the Gaussian peak-fitting; (c) quantified Sm composition (mole-fraction) as a function of distance (unit cell) across the boundary. The error-bars in (c) at each data point represent three times standard deviation, based on Gaussian statistics.

Figures:

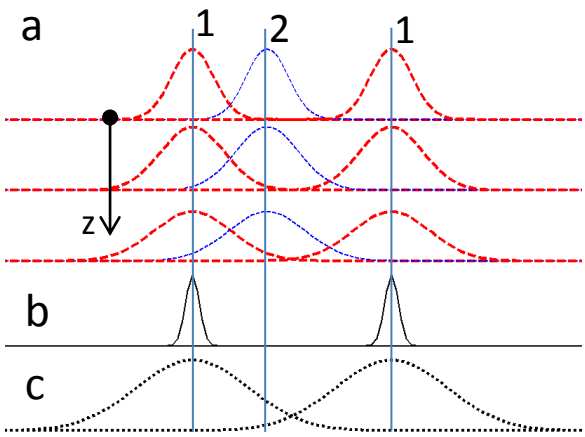

Fig.1. Schematic showing the X-ray generation process in STEM-EDS: (a) Gaussian electron probes at different thickness (z) – beam broadening along z is illustrated, and position 1 is at the atomic column site and position 2 is away from the site; (b) effective EDS scattering potential localized at atomic column and (c) overall X-ray profile obtained by the convolution of the electron wave with the EDS scattering potential at different thicknesses and by integrating the contribution through the sample thickness.

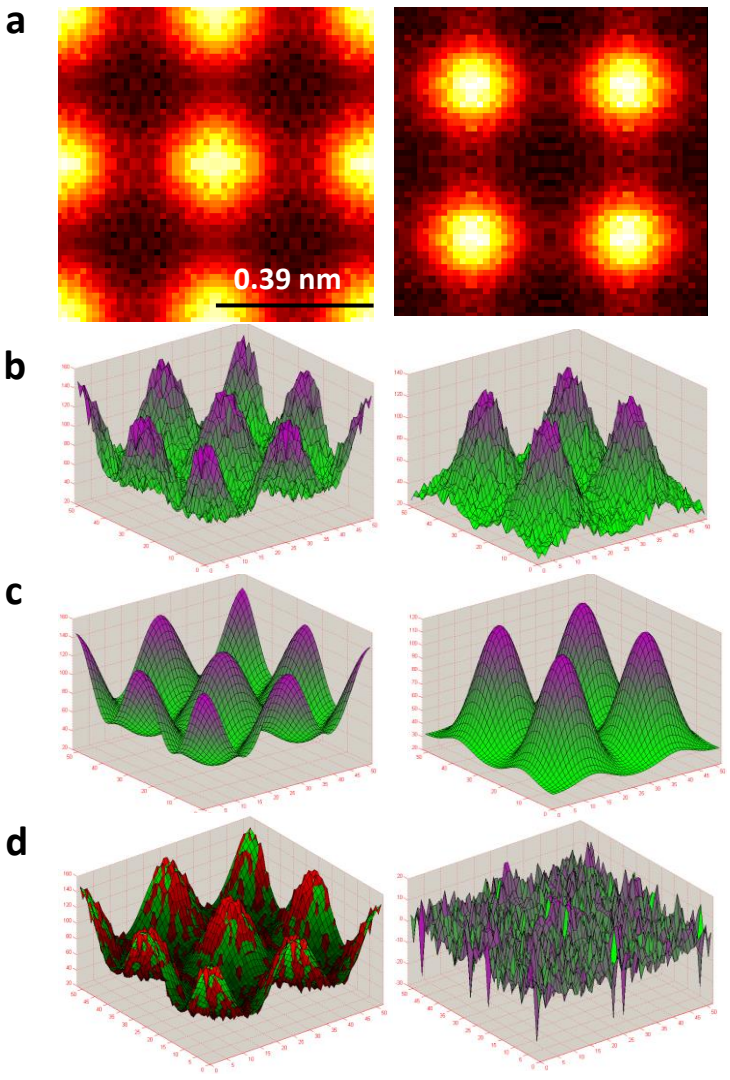

Fig.2: (a) Sr L_α EDS map (left image) and Ti K_α EDS map (right image) extracted from STEM-EDS spectral imaging; (b) experimental and (c) Gaussian peak-fitted 3-D surface plot of Sr L_α map (left image) and Ti K_α (right image) map; (d) 3-D surface plot of experimental (red) and Gaussian peak-fitted (green) Sr L_α map (left image) and of the residual from the Gaussian fitting for Sr L_α map (right image).

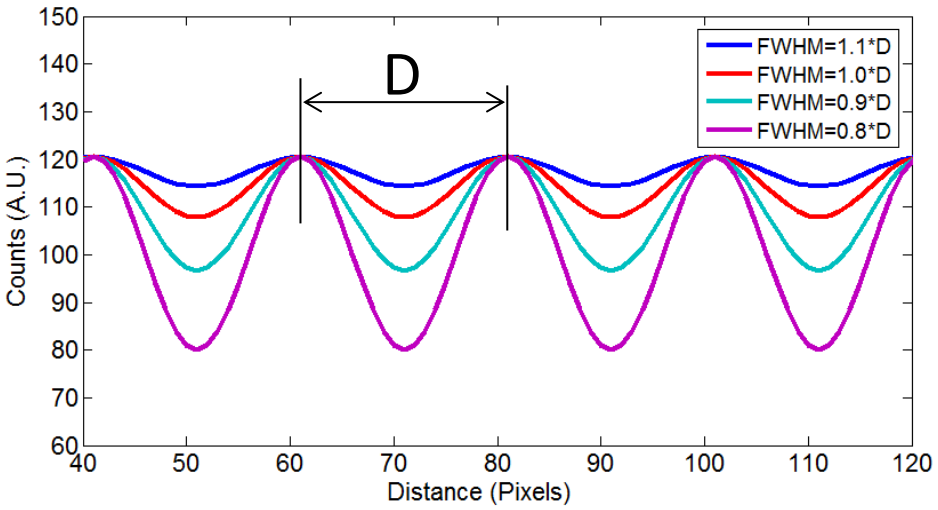

Fig.3. EDS line-profiles calculated as a function of the Gaussian peak-width defined by FWHM. The Gaussian peaks are fixed periodically at the lattice sites at a distance D apart.

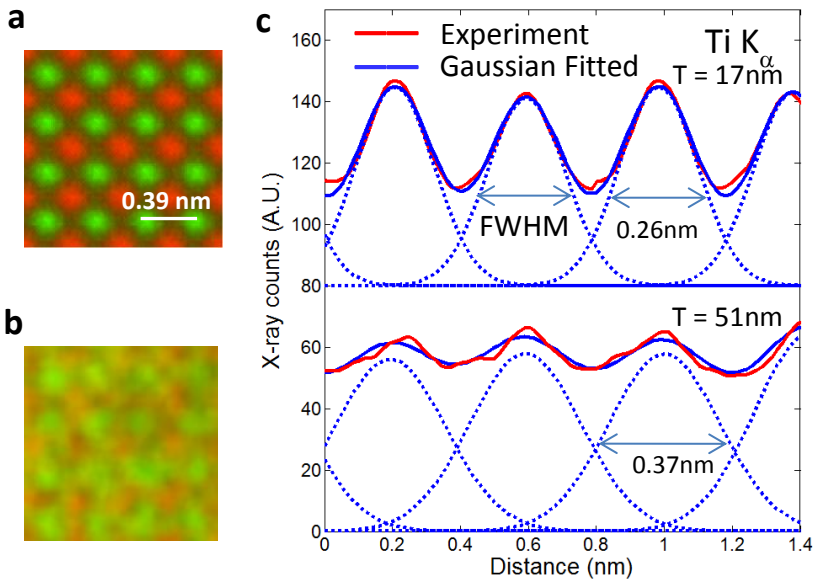

Fig.4. EDS color-map of Sr (red) and Ti (green) obtained under identical experimental conditions from (a) a 17 nm-thin and (b) a 51nm-thick STO specimen in [001]; (c) Ti experimental EDS line-profiles along [100] direction, along with the Gaussian peak-fitted Ti line-profiles under two specimen thicknesses. The dashed lines in (c) are the individual Gaussian peaks located at the lattice sites obtained from the fitting.

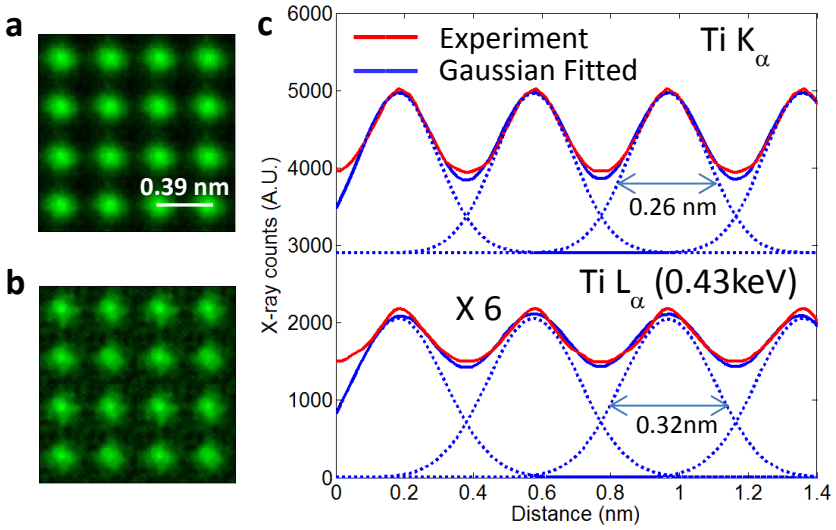

Fig.5. Ti EDS map (green) extracted using (a) Ti K_α and (b) Ti L_α; (c) Experimental EDS line-profiles along [100] direction, along with the Gaussian peak-fitted line profiles obtained using two kinds of Ti X-ray lines. The dashed lines in (c) are the individual Gaussian peaks located at the lattice sites obtained from the fitting.

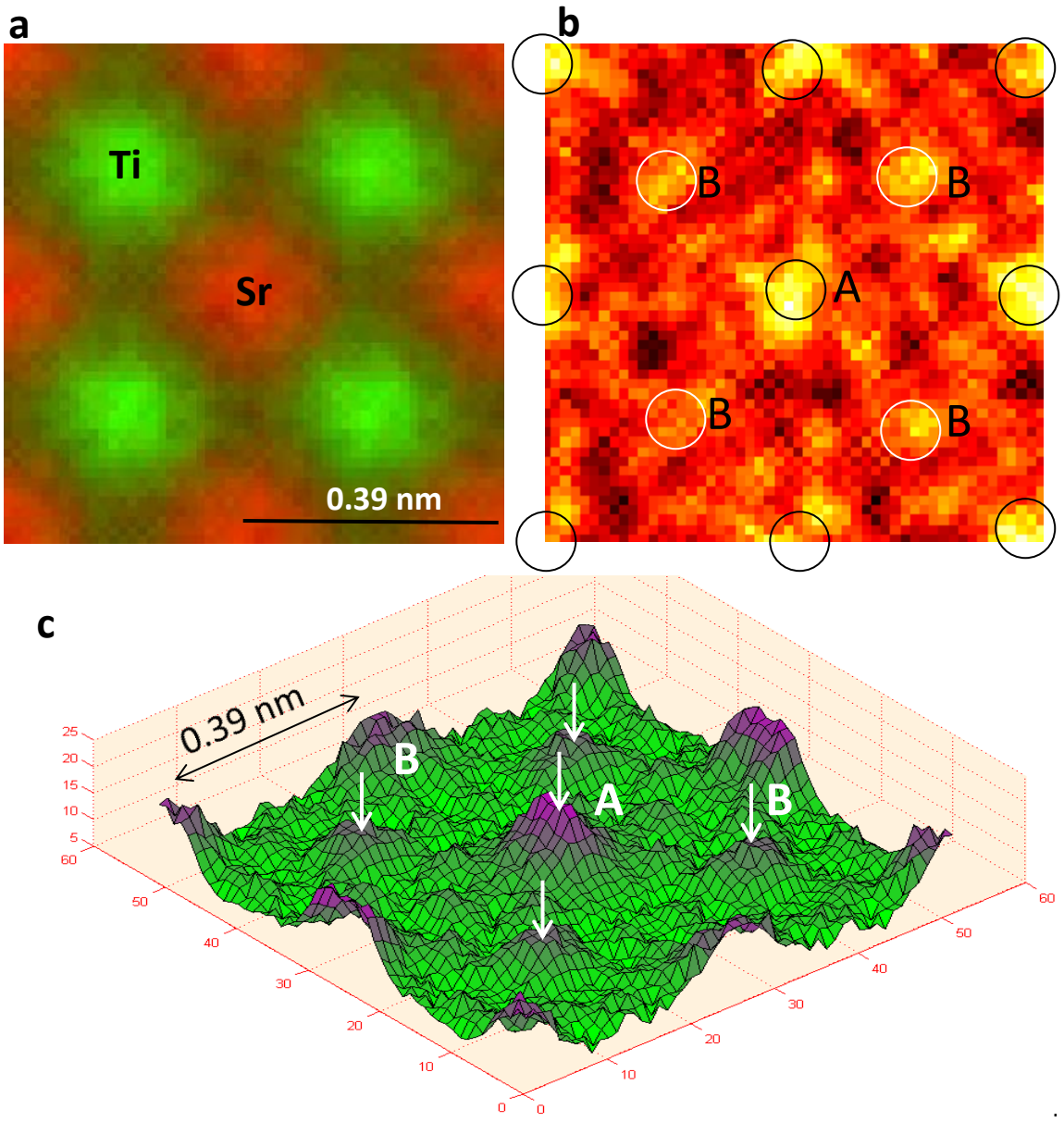

Fig.6. (a) EDS color-map of Sr (red) and Ti (green); (b) EDS map of Sm; and (c) 3-D surface plot of Sm EDS map. The arrows in (c) mark the positions of A- and B-sites in STO structure in [001] direction.

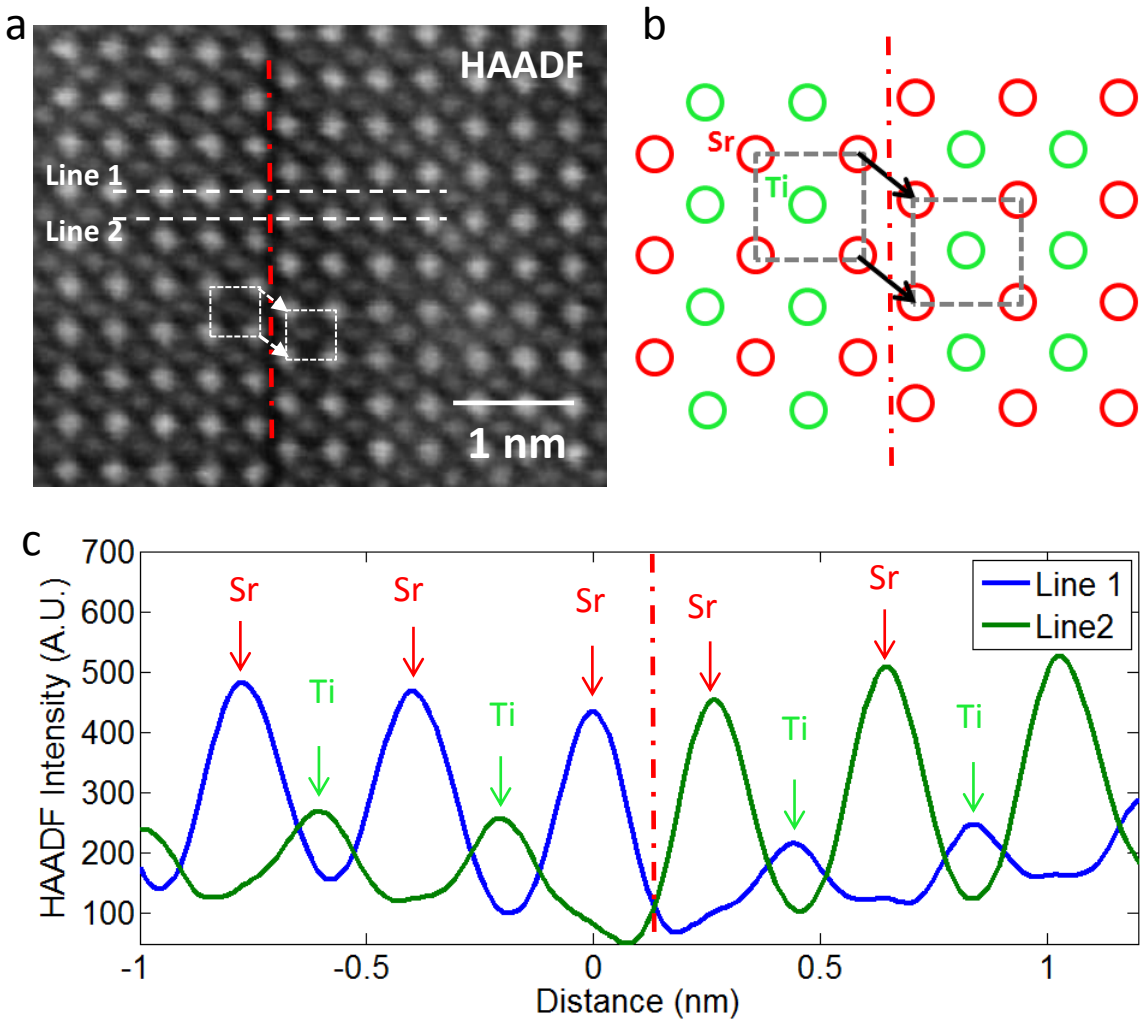

Fig.7. (a) HAADF image of antiphase boundary; (b) schematic model of the antiphase boundary; and (c) the line-profiles of HAADF intensity along lines 1 and 2 marked in (a) showing the HAADF intensities at both Sr and Ti sites increase gradually as it moves away from the boundary.

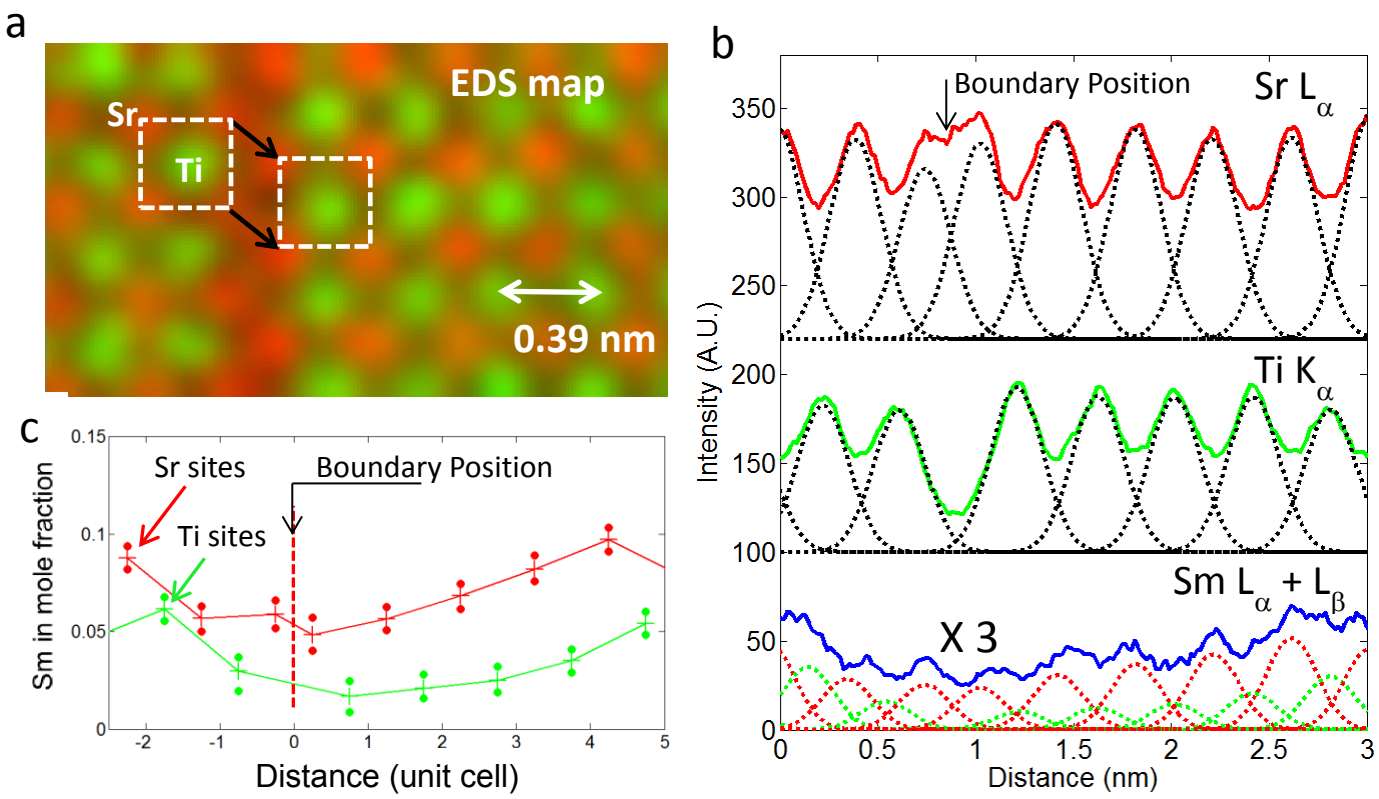

Fig.8. (a) Color-map of Sr (red) and Ti (green) showing the structure of the antiphase boundary; (b) the line-profiles of Sr, Ti and Sm EDS maps across the boundary along with Gaussian peaks (dashed-lines) located at the lattice sites resulting from the Gaussian peak-fitting; (c) quantified Sm composition (mole-fraction) as a function of distance (unit cell) across the boundary. The error-bars in (c) at each data point represent three times standard deviation, based on Gaussian statistics.